*Article*

# Preparation of Ni/$Y_2O_3$/Polylactic acid composite

**Tilen Švarc [1], Matej Zadravec [1], Žiga Jelen [1], Peter Majerič [1], Blaž Kamenik [1], Timi Gomboc [1], Janez Slapnik [2], Rajko Bobovnik [2] and Rebeka Rudolf [1,*]**

[1] University of Maribor, Faculty of mechanical engineering, Smetanova ulica 17, 2000 Maribor, Slovenia
[2] Faculty of Polymer Technology, Ozare 19, 2380 Slovenj Gradec, Slovenia
* Correspondence: rebeka.rudolf@um.si

**Abstract:** This study demonstrates the successful synthesis of Ni/$Y_2O_3$ nanocomposite particles through the application of ultrasound-assisted precipitation using the Ultrasonic Spray Pyrolysis technique. The particle size was predicted accurately using a modified equation, and they were collected in a water suspension with Polyvinylpyrrolidone (PVP) as the stabiliser. The presence of the $Y_2O_3$ core and Ni shell was confirmed with Transmission Electron Microscopy (TEM) and with electron diffraction. The TEM observations revealed the formation of round particles with an average diameter of 466 nm, while the lattice parameter on the Ni particle's surface was measured to be 0.343 nm. The Ni/$Y_2O_3$ nanocomposite particle suspensions were lyophilized, to obtain a dried material that was suitable for embedding into a Polylactic acid (PLA) matrix. The resulting PLA/Ni/$Y_2O_3$ composite material was successfully extruded successfully, so that a 3D printed technology Fused Filament Fabrication could be used further for the production of tensile test tubes. The tensile tests showed that the addition of lyophilised Ni/$Y_2O_3$ into the PLA matrix decreased the tensile strength by 21.8 %, while the tensile modulus was not influenced. Dynamic Mechanical Analysis (DMA) showed that the addition of the Ni/$Y_2O_3$ particles increased the glass transition temperature by 5 °C, and increased the storage modulus in the glass transition range significantly. These findings demonstrate the potential for utilising Ni/$Y_2O_3$ nanocomposite particles in 3D printing applications, and warrant further exploration of their mechanical properties and potential applications in various fields.

**Keywords:** Ultrasound Spray Pyrolysis, Ni/$Y_2O_3$, nanocomposite, lyophilization, extrusion, PLA, FDM 3D printing

## 1. Introduction

Nickel (Ni) is a strategic metal with catalytic properties, used mainly in organic reactions, since many transformations in organometallic chemistry are catalysed by nickel [1]–[4]. Experiments show that the Ni matrix in composite coatings is more active than a pure Ni coating [5]–[7].

Islam et al. [8] and Sun et al. [9] found that oxygen mobility at the surface of nanocrystalline $Y_2O_3$ supports an Ni electrode, which is the most commonly used electrode, plays a crucial role in the oxidative steam reforming of lignocellulosic biomass, or ethanol to hydrogen over a nickel yttrium oxide (Ni/$Y_2O_3$) catalyst. Li et al. discovered that Ni on a $Y_2O_3$ support provides remarkably efficient catalysis for $CO_2$ methanation [10]. Similarly, Taherian et al. [11] showed that nickel catalysts on yttria supports are as effective as more expensive commercial catalysts in reforming $CO_2$ and methane to syngas.

According to the research work of Guo et al. [12], they showed that catalytic activity is related closely to particle size, which means that smaller particles do not necessarily provide better catalytic activity. It can be concluded that the particle size and the volume-specific surface area are important properties that have a crucial influence on the functional properties of the materials, especially in the case of nanoparticles.

 doi:10.20944/preprints202305.2242.v1



There are many known methods for the synthesis of nanoparticles, but they are generally divided into two groups. The so-called "bottom-up" and "top-down" approaches. One subgroup of the "bottom-up" approaches are known as Spray Pyrolysis (SP) methods. SP methods are widespread in the synthesis processes of various powders and particle suspensions on the microscale and nanoscale. Spray Pyrolysis methods consist of five stages: (I) Precursor preparation, (II) Precursor aerosol generation, (III) Aerosol transport, (IV) Particle synthesis, and (V) Particle collection [13], [14]. Precursor solutions that are appropriate for SP methods are metal salts (acetates, bromides, chlorides, hydroxides, nitrates, sulphides) dissolved in water or alcohol [15]–[17]. The precursor characteristics (concentration of the salt, viscosity, density and surface tension) affect the aerosol size distribution and quantity, which, in turn, has a direct impact on particle size and morphology [18].

Ultrasonic Spray Pyrolysis (USP) is a subset of Spray Pyrolysis methods that uses a piezoelectric crystal as the nebuliser for the purpose of aerosol generation. This method was previously used in our research to synthesise different metallic and oxide nanoparticles [15], [19], [28], [29], [20]–[27]. Ultrasonic nebulisers have the advantage of narrow aerosol size distribution, which results in well controlled particle size distributions [14]. Nebulisers based on ultrasound are favoured because of their good energy-efficiency in aerosol generation compared to other available techniques [30]. As a result of cavitation and surface waves, standing waves are formed on the fluid`s surface. When the amplitude of the wave is high enough droplets break of the wave`s peak, resulting in aerosol generation [30]. The precursor aerosols are transported with the help of an inert or reaction carrier gas into the tube reactor, where synthesis occurs. During the particle synthesis, each precursor aerosol is subjected to several physical and chemical processes, such as the evaporation of the solvent liquid, precipitation of the salt, pyrolysis, reduction reactions, and, finally, drying of the formatted nanoparticles [13], [31]. Due to the high homogeneity of the precursor solution, the created particles have mostly a controlled stoichiometric ratio and morphology [18], [32]. High temperatures in the tube reactor cause rapid evaporation of the solvent, which results in high surface-to-volume ratio particles. Collection of the nanoparticles is commonly carried out with gas filtration methods: electrostatic filters, or liquid washing in collection bottles with stabilising agents [31].

The implementation of ultrasound for droplet generation in Spray Pyrolysis presents an upscale ready process for nanomaterial synthesis, since it operates continuously, and has a good control of the particle size and composition [33], [34]. The USP method has a good potential to eliminate technological problems of nanoparticles` size variations and provides a more controlled nanoparticle synthesis [27], [35], [36]. In most cases, nanoparticles synthesised by the USP method are collected in the form of a suspension, so it is necessary to dry the suspension to obtain nanoparticles in powder form. The process of lyophilisation is used widely for drying nanoparticles in pharmaceuticals [37], [38]. To ensure a successful drying process, the nanosuspensions are dried in multiple steps. This involves a freezing phase, during which the nanosuspension is frozen and the solvent is converted into a crystalline or amorphous solid. Subsequently, the drying phase occurs, with a rapid pressure drop in the system. USP coupled with lyophilisation offers a green chemistry approach, as there are no significant pollutants or hazardous chemicals present at the end of the process.

The mechanism of $Ni/Y_2O_3$ nanocomposite particles` synthesis with USP was proposed in our previous research [15]. In the reactor part of the USP device water evaporation takes place first, and then the dried droplets enter the high-temperature area. Initially, thermal decomposition of the yttrium nitrate and nickel nitrate occurs, leading to the formation of yttrium oxide and nickel oxide. As yttrium oxide is significantly more stable than nickel oxide, a hydrogen reaction can only take place for the formation of nickel. Thus, $Ni/Y_2O_3$ can only be produced following the dehydration and thermal decomposition of metal nitrates, with the hydrogen reduction of nickel oxide being achievable solely in an $H_2/N_2$ atmosphere.

 doi:10.20944/preprints202305.2242.v1



Utilizing Ni/$Y_2O_3$ nanocomposites in a Polylactic acid (PLA) matrix, with the ability for 3D printing, presents new possibilities for using this composite material for catalytically induced reactions, such as carbon monoxide methanation [8], [9]. The 3D printing aspect shows new approaches for producing filters, mesh-like converters, or other complex shapes, where the passing CO and $CO_2$ gases, with the addition of $H_2$, are converted into methane, as a measure for removing carbon oxides from process gases. The potential high efficiency of the small Ni/$Y_2O_3$ particle methanation in a 3D printed PLA/Ni/$Y_2O_3$ composite could be used as an alternative for CO removal from hydrogen-rich gas streams used as fuel for polymer electrolyte fuel cells. Usually, the CO removal is done by diffusing the hydrogen-rich gas through a Pd–Ag membrane at high temperatures, or by metal catalysts, such as Au, Pt, Ni, Ru and Rh, on metal oxide substrates of $Al_2O_3$, $SiO_2$, $TiO_2$, or $ZrO_2$ [39].

In our research, the Ni/$Y_2O_3$ nanocomposite gains potential according to its specific nickel and yttrium properties, to increase the mechanical properties of PLA as one of the currently most common materials produced from renewable resources. The synthesised Ni/$Y_2O_3$ nanocomposite can be used in many fields. One of the applications is the production of ink suitable for application to various surfaces. Such deposits can be used as catalysts in green chemistry applications, since nickel has good catalytic properties in organic reactions [2]. Nickel with the addition of yttrium oxide has been shown to be a good catalyst for the production of hydrogen from ethanol and the methanation of carbon dioxide [40]. Compared to other commonly used catalysts like platinum, nickel delivers a similar performance at a significantly lower cost [41].

## 2. Materials and Methods

### *2.1. Materials*

The chemicals used to prepare the precursor solution for the USP synthesis were nickel(II) nitrate (Sigma-Aldrich, Germany) and yttrium(III) nitrate (Sigma-Aldrich, USA). During the synthesis process, Polyvinylpyrrolidone (PVP) (Sigma-Aldrich, China) with the average molar mass of 40,000 g/mol was used to stabilise the nanocomposite particles, and PLA (NatureWorks LLC, USA) was used as the matrix.

### *2.2 Nanocomposite particle synthesis*

#### 2.2.1. Ultrasound spray pyrolysis

The concentration of nickel(II) nitrate in the precursor solution was 0.025 mol/L, and the concentration of yttrium(III) nitrate was 0.100 mol/L. The solvent was de-ionised water. The impact of the precursor concentrations was studied previously [15].

The precursor aerosol formation occurred in the ultrasound generator, which uses a piezoelectric crystal to form ultrasonic waves at 1.65 MHz. Nitrogen was used as the carrier gas (1 L/min) and hydrogen as the reaction gas (1 L/min). The reactor tube inner diameter was 40 mm, the length of the evaporation zone and the reaction zone was 1 m. The temperature in the evaporation zone was 200 °C and 900 °C in the reaction zone.

The final size of the nanocomposite particle is strongly dependent on the initial droplet size and precursor solution concentration. The correlation between ultrasonic frequency and the mean droplet diameter was presented by Lang [42], equation 1. An equation for particle size prediction was developed previously for USP synthesis [43], equation 2.

$$\mathrm{d} = 0.34\sqrt[3]{\frac{8\pi\gamma}{\rho_{sol}f^2}}, \quad (1)$$

$$\mathrm{D} = d\sqrt[3]{\frac{C_{sol}M_{par}}{\rho_{par}M_{pre}}}, \quad (2)$$

 doi:10.20944/preprints202305.2242.v1



Given that the precursor solution is a low-concentration salt solution, we selected a density and surface tension for the solution equivalent to that of water. To determine the concentration of the precursor solution, hypothetical particle density, molar mass of the precursor, and hypothetical molar mass of the particles, we calculated their mass-averaged values and molar-averaged values. The average particle size was calculated using both mass-averaged and molar-averaged values, which yielded values of 491 nm and 483 nm, respectively. As there was no significant deviation between the two, their average value, 487 nm, will be used for further comparison.

Three collection bottles with 500 mL de-ionised water and PVP were used to collect the synthesised nanocomposite particles. The concentration of PVP was 5.00 g/L. Two batches of USP synthesis were carried out, with each batch taking 3 hours to complete.

#### 2.2.1 Lyophilisation

Lyophilisation was performed using an LIO-2000 FLT lyophiliser, produced by Kambič, Slovenia. The lyophilisation protocol used in this study consisted of a freezing period of 5 hours and 30 minutes at –35 °C, followed by a drying period when the pressure was reduced to 0.175 mbar and the temperature was raised to 20 °C. The vacuum at 20 °C was maintained for 20 hours to complete the drying process. This protocol was designed carefully to ensure the effective removal of water and preservation of the sample's structure and properties.

PVP was used as a cryoprotectant and stabiliser during the freeze-drying process, to help preserve the integrity of the Ni/$Y_2O_3$ and prevent agglomeration and sedimentation. It forms a protective layer around the material, shielding it from damage caused by freezing, dehydration and drying. Additionally, PVP can help maintain the physical and chemical properties of more delicate materials, such as their shape, size, and activity, throughout the drying process [44]–[46].

To ensure consistent drying conditions across all samples, the samples with varying PVP concentrations were freeze-dried in R6 vials equipped with thermocouple attachments, to enable temperature measurement at the bottom of the vial. These measures were taken to minimise variations and ensure accurate and reliable results. In addition, a larger batch of material was dried in a metal tray, to increase the amount of material that could be processed at once.

### *2.3. Composite preparation*

#### 2.3.1. Extrusion process

The lyophilised Ni/$Y_2O_3$ nanocomposite with 5.00 g/L PVP was mixed directly with the PLA granulate, that was dried at 80 °C for 4 h, see Figure 1. The mass ratio of PLA and Ni/$Y_2O_3$ was 100:2. The extrusion process was carried out in two steps using a parallel twin-screw extruder (Thermo Fisher Scientific). In the first step compounding of the PLA granulate and Ni/$Y_2O_3$ nanocomposite took place, followed by one more extrusion of the previously prepared PLA/Ni/$Y_2O_3$ composite granules into a 3D printing filament for Fused filament fabrication (FFF). The two step extrusion ensured a homogenised material. The same extrusion process was repeated for the pure PLA granulate, with the goal to obtain a reference material.

 doi:10.20944/preprints202305.2242.v1




**Figure 1.** PLA granulate with $Ni/Y_2O_3$ nanocomposite particles.

2.3.2. FFF 3D printing

The FFF 3D printer, Raise3D N2, was used to print tensile test specimens type 1BA in accordance with ISO 527-2 [47]. The parameters of the 3D printing were as follows: Nozzle temperature was 215 °C, bed temperature was 60 °C, 100 % infill and 110 % first layer, 50 % overlapping with a "lines" pattern. The diameter of the filament was 1.700 mm. Neat PLA test specimens were 3D printed to serve as reference material.

*2.4. Nanocomposite characterization methods*

2.4.1. Transmission electron microscopy

Transmission Electron Microscopy (TEM) with Energy Dispersive X-ray (EDS) was used to evaluate the state of the nanocomposite particles in the lyophilised state. A Jeol JEM 2100 was used with a 200 kV $LaB_6$ electron source.

The size distribution was obtained by measuring the particle size on the TEM images. A total of 200 particles were measured. The data were evaluated with ImageJ software [48].

2.4.2. Viscosity and drying times

The viscosity of the nanocomposite suspensions with different PVP concentrations was measured using MCR (Anton Paar). The $Ni/Y_2O_3$ nanocomposite suspension, obtained via USP synthesis, had PVP added to achieve the following PVP concentrations: 2.50 g/L, 5.00 g/L, 10.00 g/L and 20.00 g/L. In addition, a water-based solution containing PVP at the same concentrations was used as a baseline for comparison with the nanocomposite suspension, to assess the influence of the nanocomposite particles on the suspension. The same $Ni/Y_2O_3$ nanocomposite suspension were used to determine the length of the drying process.

*2.5. PLA $Ni/Y_2O_3$ composite characterization methods*

2.5.1. Mechanical properties

A tensile test and Dynamic Mechanical Analysis (DMA) were utilised to attain the mechanical properties of the PLA/$Ni/Y_2O_3$ composite. The tensile test was conducted on a Shimadzu AG-X Plus 10 kN in accordance with ISO 527-1 [49], and the samples were 3D printed type 1BA test specimens. The Tensile modulus was evaluated in the interval between 0.05 % and 0.25 % strain. The DMA was performed on a Perkin Elmer DMA 8000 in accordance with ASTM D5418 [50], with a 1 Hz frequency and a 0.02 mm amplitude. For each material five repetitions for tensile tests were conducted, and two for DMA.

 doi:10.20944/preprints202305.2242.v1



2.5.2. Scanning electron microscopy

A Scanning Electron Microscope (SEM), Sirion 400 NC (FEI Sirion 400 NC, FEI Technologies Inc., Hillsboro, USA), with an EDS INCA 350 (Oxford Instruments, UK), was used for the SEM investigations of the fracture of the prepared PLA Ni/$Y_2O_3$ composite that was tested on the tensile test.

## 3. Results and discussion

*3.1. Transmission electron microscopy*

The TEM images obtained in this study offer important insights into the Ni/$Y_2O_3$ nanocomposite particles. As shown in Figure 2, the images revealed a high level of roundness at lower magnifications. However, an undulated surface can be observed at higher magnifications, as seen in Figure 4, which is the result of small particles in the size range of 10 nm that were sintered and formed the round Ni/$Y_2O_3$ nanocomposite particles. These particles were enfolded, and their size can only be determined by observing their grain orientation. This detailed information on the size, shape and distribution of the nanoparticles can provide valuable guidance for further research and development of nanocomposite materials.

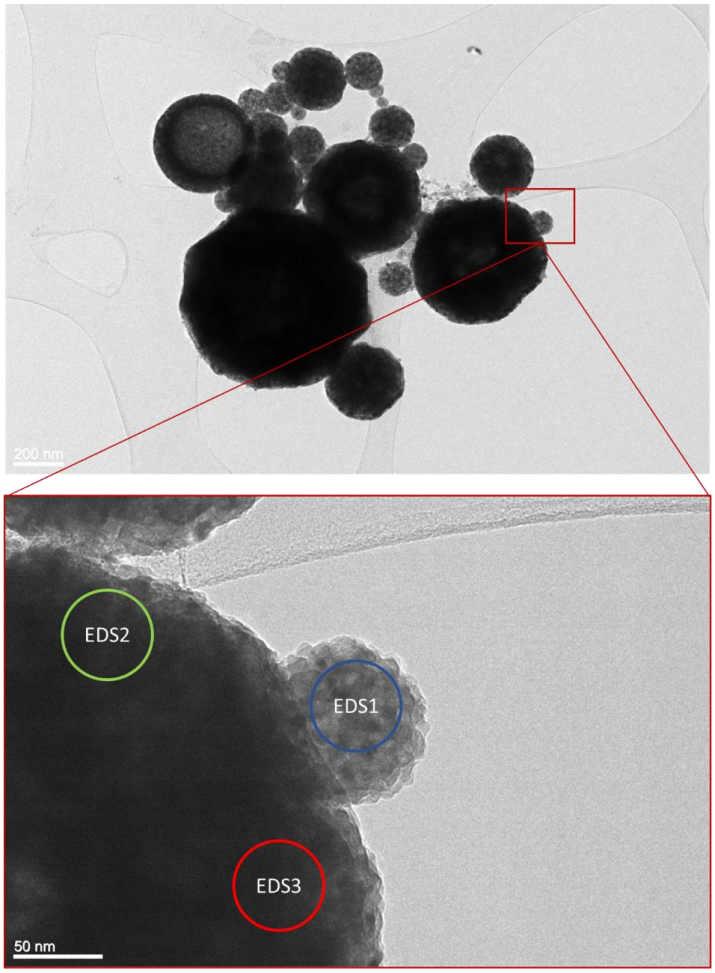


**Figure 2.** TEM microstructure of the Ni/$Y_2O_3$ nanocomposite particles.

The real particle number weighted particle size was measured to be 466 nm. The smallest observed non-agglomerated particle had a diameter of 55 nm, while the largest had a diameter of 1603 nm. The relative frequency of particles by size is presented in

 doi:10.20944/preprints202305.2242.v1



Figure 3. Slightly over half of the particles are in the size range of 100 nm to 500 nm, while 34 % fall between 500 nm and 1000 nm. The smallest particles, below 100 nm, comprise only 5.2 % of the total. The remaining particles are larger than 1000 nm.

The calculated particle diameter obtained using equations 1 and 2, which was 487 nm, and the measured average particle diameter of 466 nm, show good agreement. This shows that the equations presented previously in [42] can be used to predict the particle size of Ni/$Y_2O_3$ nanocomposite particles. Further study is needed to determine the applicability to the general area of metallic and ceramic composite particles produced by USP.

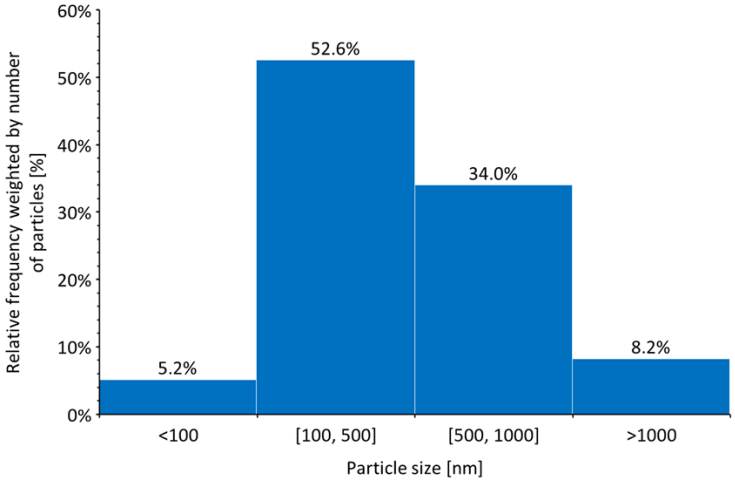


**Figure 3.** Ni/$Y_2O_3$ nanocomposite particles size distribution weighted by number of particles.

Figure 4 provides a detailed view of the crystal lattice on the surface of the Ni/$Y_2O_3$ nanocomposite particles. By comparing the measured distance between the crystal planes, which was 0.344 nm and 0.343 nm, with the theoretical distance between crystal planes in cubic face-centered nickel, which was 0.348 nm, we can confirm the presence of cubic nickel on the particle surface. This information confirms the mechanism established previously [15], which proposed the formation of elemental nickel on the surface of the Ni/$Y_2O_3$ nanocomposite particles.

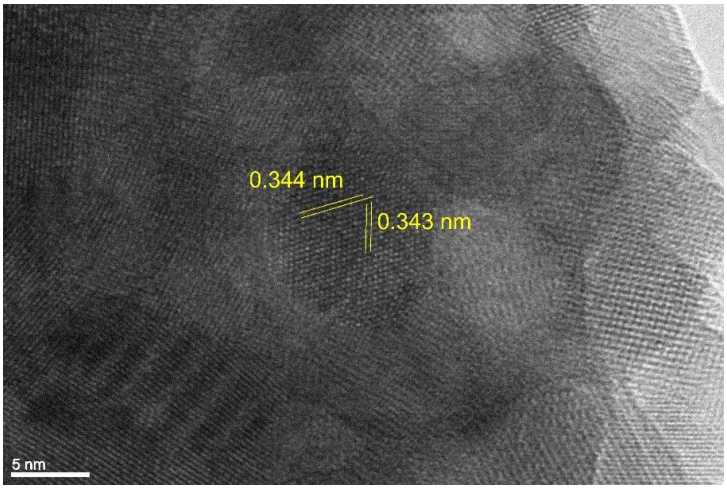


**Figure 4.** Crystal lattice structure on the Ni/$Y_2O_3$ nanocomposite particle surface.

Electron diffraction is a powerful tool used for investigation of the material structure at the atomic level. With it we can analyse the patterns of electron diffracted by a crystal,

 doi:10.20944/preprints202305.2242.v1



and determine the crystals` arrangement of atoms and their spacing withing the crystal lattice. Figure 5 shows the electron diffraction of the Ni/$Y_2O_3$ nanocomposite particles. Great agreement can be observed between the experimental and the theoretical diffraction image of yttrium oxide. Therefore, we can confirm the presence of yttrium oxide in the nanocomposite core.

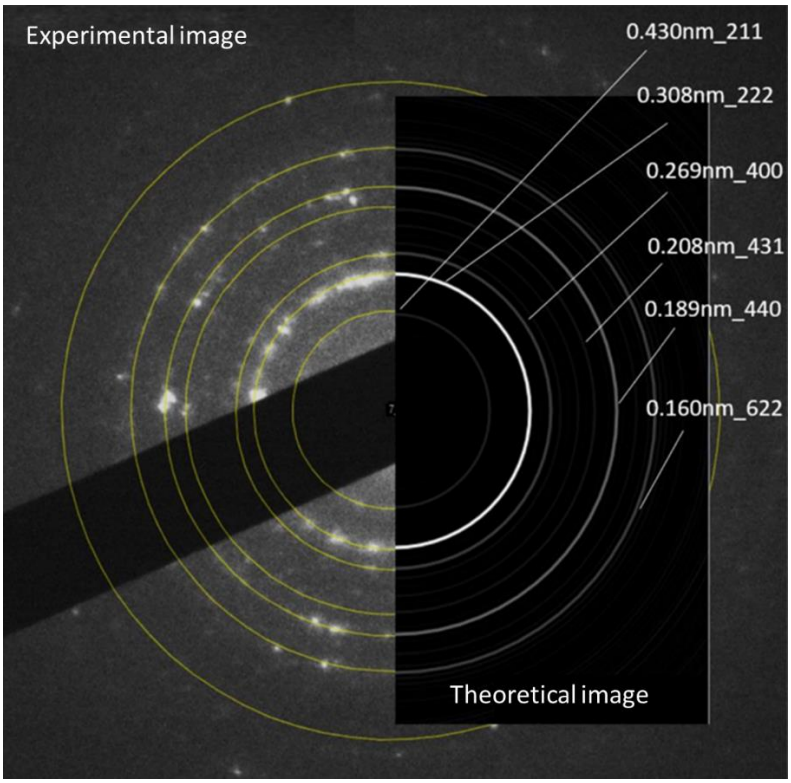


**Figure 5.** Electron diffraction of the Ni/$Y_2O_3$ nanocomposite particles; experimental and theoretical image.

EDS provides valuable information on the chemical makeup of materials, which is crucial for understanding their properties and potential applications. EDS analysis was performed to investigate the elemental composition of the Ni/$Y_2O_3$ nanocomposite particles. Figure 2 and Table 1 present the results of the analysis, showing the presence and relative abundance of various elements in the sample. By comparing the ratio between Ni- and Y-nitrate in the precursor solution and the ratio between Ni and Y in the nanocomposite particles obtained from the EDS analysis, it is pointed out that there is some material loss during USP synthesis, observed especially on the Ni side. This loss may potentially occur due to deposition on the reactor walls and variations in the reaction rates between Ni and Y ions.

No significant difference in the composition of smaller and larger particles can be observed, as shown in Figure 2 and Table 1. Although the nanocomposite particles have a low At% of Nickel, there is a sufficient amount of Ni present to produce a noticeable colour shift into grey in the 3D printed material when compared to pure PLA (Figure 9). The observed colour shift can be attributed to the presence of Ni in the nanocomposite particles, as Yttrium Oxide is white, and, thus, unlikely to contribute to such a colour change.

 doi:10.20944/preprints202305.2242.v1



**Table 1.** EDS analysis of the Ni/$Y_2O_3$ nanocomposite particles.

| Element | EDS 1 [at. %] | EDS 2 [at. %] | EDS 3 [at. %] |
|---|---|---|---|
| O | 54.09 | 51.35 | 57.95 |
| Ni | 5.16 | 7.19 | 3.04 |
| Y | 40.75 | 41.46 | 39.01 |
| Total | 100.00 | 100.00 | 100.00 |

*3.2. Viscosity and drying time*

Viscosity has a direct effect on the rate of particle settling. Higher viscosity results in slower particle settling rates, and lower viscosity results in faster settling rates. The viscosity of the fluid medium has a major influence on the drag force experienced by particles, which affects the settling velocity of the particles directly. As viscosity increases, the drag force experienced by the particles also increases, causing them to settle at a slower rate [51]. When PVP is added to water, it increases the viscosity of the solution. This is due to the formation of a three-dimensional network of polymeric chains, which leads to increased interactions between water molecules and reduced mobility of the molecules. The viscosity is increased as a result [52], [53].

The addition of Ni/$Y_2O_3$ particles did not impact the viscosity of the suspensions significantly, while the viscosity was affected significantly by the concentration of PVP. The viscosity values of the suspensions at different PVP concentrations are presented in Table 3.

**Table 2.** Impact of PVP and Ni/$Y_2O_3$ nanocomposite particle on the suspension viscosity.

| PVP concentration [g/L] | Viscosity of water [mPa·s] | Viscosity of Ni/$Y_2O_3$ particles suspension [mPa·s] |
|---|---|---|
| 0.0 | 0.8±0.05 | 0.82±0.04 |
| 2.5 | 0.90±0.01 | 0.92±0.04 |
| 5.0 | 0.98±0.05 | 0.98±0.04 |
| 10.0 | 1.10±0.07 | 1.05±0.06 |
| 20.0 | 1.36±0.05 | 1.42±0.13 |

Higher viscosity solutions tend to require longer drying times, resulting in reduced product yields. Therefore, it is important to control the viscosity of the solution, in order to optimise the lyophilisation process. The figures show the effect of PVP concentration in water on the viscosity of it, as well as the impact of the presence of Ni/$Y_2O_3$ particles on the viscosity.

The freezing time was not affected significantly by varying the concentrations of PVP. However, the drying time was impacted notably, as illustrated in Figure 6. The drying time was defined as the duration between the temperature increase and the point when the sublimation front reached the bottom of the vial. The drying times for each suspension are shown in Table 3. The impact of additional PVP in the solution was more pronounced at lower PVP concentrations, 2.50 g/L and 5.00 g/L, while additional increases do not affect the drying times significantly.

The results show that the drying time increased as the concentration of PVP increased from 2.50 g/L to 5.00 g/L, indicating that lower PVP concentrations have a shorter drying time. However, as the PVP concentration increased to 10.00 g/L and 20.00 g/L, the drying time did not exhibit significant changes, indicating that there might be an optimal concentration range for PVP that balances the cryostabilisation effect, stabilisation effect and drying time. From our range of data it is indicated that this concentration is close to 5.00 g/L, therefore, this concentration of PVP was used in the Ni/$Y_2O_3$ suspensions in all subsequent freeze-drying processes and the PLA/Ni/$Y_2O_3$ composite preparation.

Preprints (www.preprints.org) | NOT PEER-REVIEWED | Posted: 31 May 2023 doi:10.20944/preprints202305.2242.v1



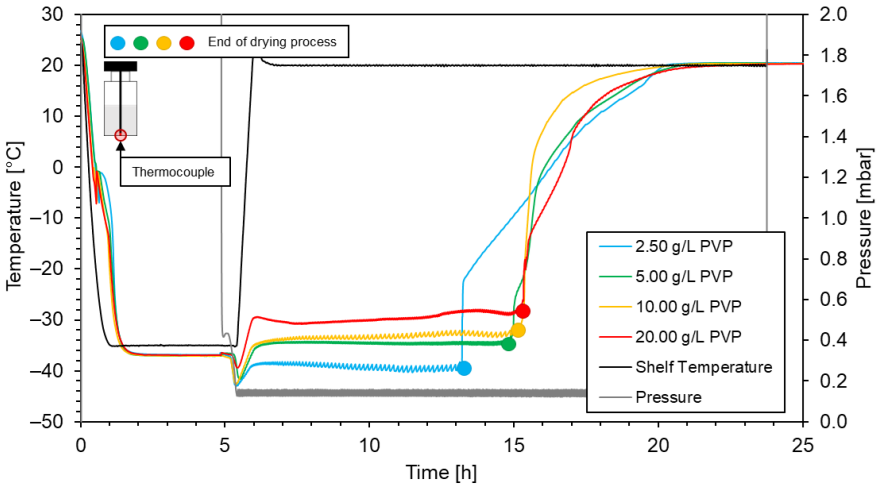


**Figure 6.** Impact of PVP concentration on the drying time of the Ni/Y2O3 nanocomposite particle suspension.

**Table 3.** Impact of PVP concentration on the drying time of the Ni/$Y_2O_3$ nanocomposite particle suspension.

| PVP concentration [g/L] | Drying time |
|---|---|
| 2.50 | 7 h 36 min |
| 5.00 | 9 h 06 min |
| 10.00 | 9 h 30 min |
| 20.00 | 9 h 48 min |

*3.3. Mechanical properties*

The incorporation of lyophilised Ni/$Y_2O_3$ into the PLA matrix resulted in decreased tensile strength from 60.0 MPa to 50.8 MPa (15.3 %) as can be seen in Figure 7. The influence of the Ni/$Y_2O_3$ particles on the tensile modulus and strain at tensile strength was not significant, while the strain at break decreased from 4.6 % for neat PLA to 3.6 % for the PLA/Ni/$Y_2O_3$ composite (Table 4). Decreased tensile strength and strain at break may result from agglomerated Ni/$Y_2O_3$ particles (see Figure 9), which act as stress concentration points, leading to premature failure.

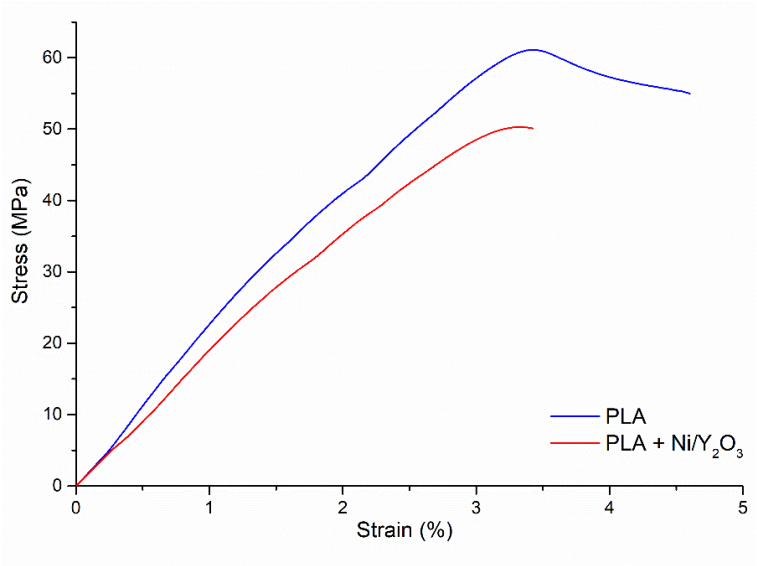


**Figure 7.** Representative strain-stress curves of PLA and PLA/Ni/$Y_2O_3$ composite.

 doi:10.20944/preprints202305.2242.v1



**Table 4.** Results of mechanical testing for the PLA and PLA/Ni/$Y_2O_3$ composite.

| Sample | Tensile modulus [MPa] | Tensile strength [MPa] | Strain at tensile strength [%] | Strain at break [%] |
|---|---|---|---|---|
| PLA | 2.62 ± 0.28 | 60.0 ± 1.1 | 3.3 ± 0.2 | 4.6 ± 0.5 |
| PLA/Ni/$Y_2O_3$ | 2.77 ± 0.32 | 50.8 ± 1.28 | 3.3 ± 0.1 | 3.6 ± 0.2 |

Although the DMA results did not reveal a significant difference in the storage modulus (*E'*) between pure PLA and the PLA/Ni/$Y_2O_3$ composite at 30 °C (Figure 8), the addition of Ni/$Y_2O_3$ particles resulted in an increase of 5 °C in the glass transition temperature. This was evident from the peak of the loss modulus (*E''*), which represents the glass transition temperature. The increased glass transition temperature was ascribed to the steric hindrance of molecular motion by the rigid Ni/$Y_2O_3$ particles. The increase in the glass transition temperature is reflected in the significant increase of *E'* in the glass transition range at 60 °C, which was 315 % higher compared to the neat PLA sample. Therefore, the addition of Ni/$Y_2O_3$ particles improved the thermal properties of the PLA matrix as it increased the usable temperature range for structural applications.

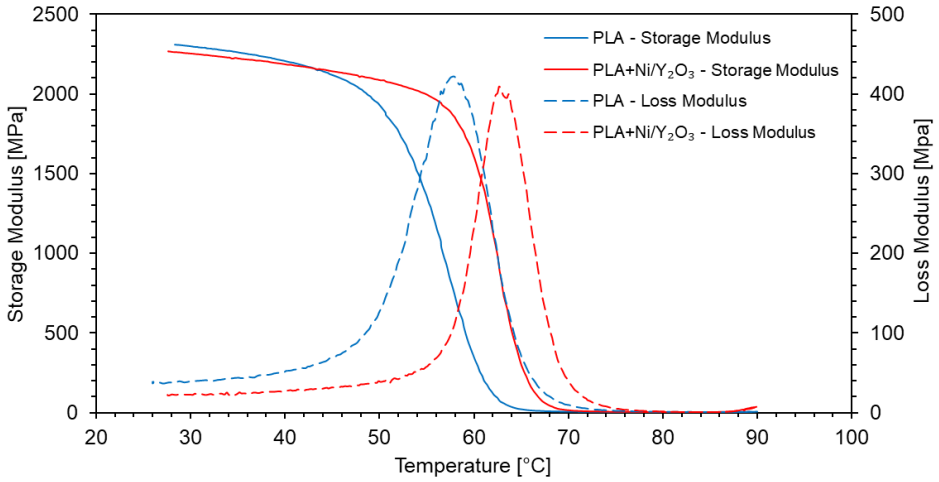


**Figure 8.** Storage Modulus and Loss Modulus as a function of temperature for PLA and PLA/Ni/$Y_2O_3$ composite.

*3.4. Scanning electron microscopy*

SEM examination of the fracture surfaces revealed that the Ni/$Y_2O_3$ particles were uniformly distributed throughout the volume of the PLA matrix. Figure 9 shows the fracture of the tensile tests tubes at three different magnifications, identifying individual agglomerated groups of particles in the PLA-Ni/$Y_2O_3$ sample. The comparison of the fracture surfaces of PLA and PLA/Ni/$Y_2O_3$ does not show similar characteristics, as the fracture facets in the case of pure PLA were significantly longer, which means that the fracture in the PLA tensile test tube was tougher compared to the PLA/Ni/$Y_2O_3$ composite. Namely, in the case of PLA/Ni/$Y_2O_3$, the SEM examination revealed significantly shorter fracture facets and smaller fracture surfaces, indicating that the fracture was more brittle, which agrees with the results of the tensile test.

Preprints (www.preprints.org) | NOT PEER-REVIEWED | Posted: 31 May 2023 doi:10.20944/preprints202305.2242.v1



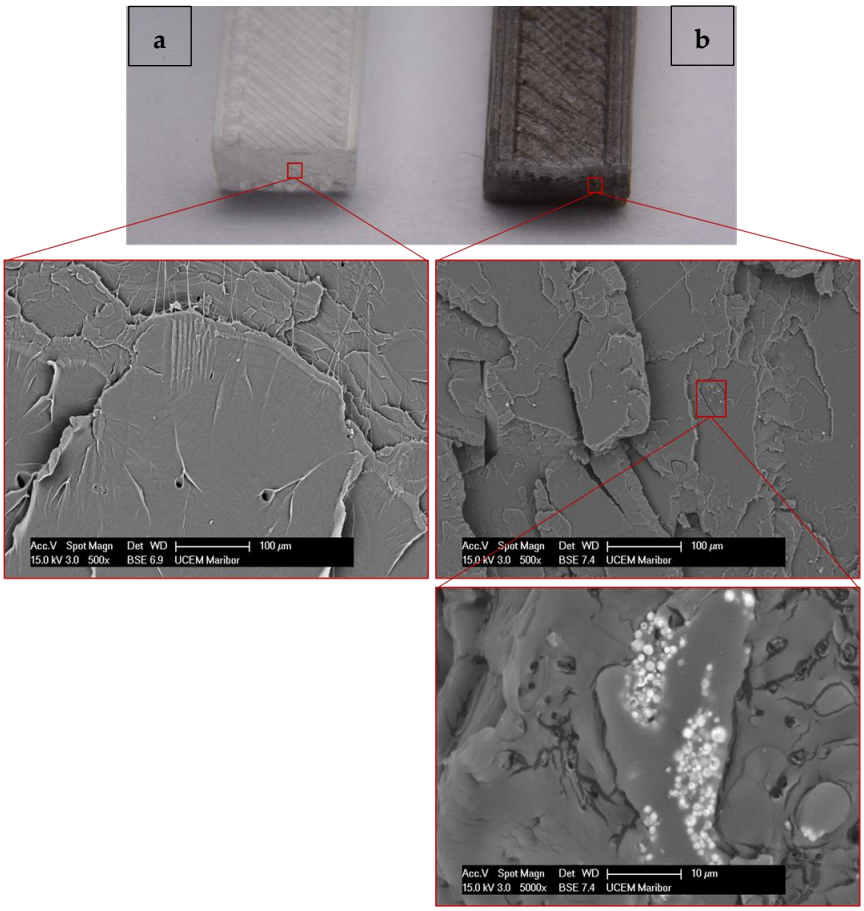


**Figure 9.** SEM microstructure of fracture for: a) PLA and b) PLA/Ni/$Y_2O_3$ composite.

These findings demonstrate the potential for utilising Ni/$Y_2O_3$ nanocomposite particles, prepared with a green chemistry technique, in 3D printing applications, and warrants further exploration of their mechanical properties and potential applications in various fields.

The successful synthesis and characterisation of Ni/$Y_2O_3$ nanocomposite particles using the USP method provides a new avenue to produce high-quality materials with potential applications in various industries. Additionally, the Ni/$Y_2O_3$ nanocomposite particle suspensions were lyophilized, to obtain a dried material that is suitable for incorporating into a suitable polymer matrix, such as PLA, that can be extruded into a 3D print ready filament.

In further research we will focus on determining the catalytic properties of Ni/$Y_2O_3$ nanocomposites and PLA Ni/$Y_2O_3$ composites, as previous research with X- ray photoelectron spectroscopy has shown non-stoichiometry [15].

## 4. Conclusions

Overall, this study contributes to the field of nanocomposite particle synthesis, PLA based filament extrusion and 3D printing technology. The following conclusions can be drawn from our research:

- The USP method proved to be a highly effective green chemistry approach in the successful synthesis of Ni/$Y_2O_3$ nanocomposite particles.
- The use of a modified, previously presented equation, allowed for accurate prediction of the particle size, which was confirmed by TEM analysis.
- The presence of the $Y_2O_3$ core and Ni shell was also confirmed with TEM and electron diffraction.

- The proper concentration of PVP in the nanoparticle suspension before lyophilisation leads to different cryostabilisation effects, stabilisation effects and optimal drying times.
- The lyophilisation process proved successful in obtaining a dried Ni/$Y_2O_3$ nanocomposite particle powder, and the PLA/Ni/$Y_2O_3$ composite material was extruded successfully and 3D printed using FDM technology.
- Tensile strength decreased with the addition of Ni/$Y_2O_3$ nanoparticles, which is the result of their agglomeration in the PLA matrix.
- The fracture surfaces are different, as the fracture facets were significantly longer in the case of pure PLA, which indicates a higher toughness of PLA compared to the PLA/Ni/$Y_2O_3$ composite.
- The addition of Ni/$Y_2O_3$ particles in PLA resulted in an increase of 5 °C in the glass transition temperature, also evident from the position of the peak of the loss modulus.

**Author Contributions:** Conceptualization, M.Z. and R.R.; methodology, M.Z. and R.R.; software, T.Š. B.K., T.G. and J.S.; validation, M.Z., J.S. and R.R.; formal analysis, T.Š., Ž.J., R.B. and J.S.; investigation, T.Š., Ž.J., P.M., B.K., J.S. and R.B.; resources, M.Z. and R.R.; data curation, M.Z. and R.R.; writing—original draft preparation, T.Š. Ž.J. and R.R.; writing—review and editing, R.R.; visualization, T.Š.; supervision, R.R.; project administration, R.R.; funding acquisition, M.Z. and R.R. All authors have read and agreed to the published version of the manuscript.

**Funding:** This research was funded by the Slovenian Research Agency Training and funding of a Young Researcher, (Co) financing agreements nos. 1000-19-0552, 1000-20-0552 and 1000-21-0552. And Research programme P2-0120.

**Acknowledgments:** Thanks go to technician Ms. Lidija Rozman Zorko for help with filament extrusion.

**Conflicts of Interest:** The authors declare no conflict of interest.

**Abbreviations:** Dynamic Mechanical Analysis (DMA), Energy Dispersive X-ray (EDS), Storage modulus ($E'$), Loss modulus ($E''$), Fused Filament Fabrication (FFF), nickel yttrium oxide (Ni/$Y_2O_3$), Polylactic acid (PLA), Polyvinylpyrrolidone (PVP), Scanning Electron Microscopy (SEM), Spray Pyrolysis (SP), Transmission Electron Microscopy (TEM), Ultrasonic Spray Pyrolysis (USP)

**Symbols:** Precursor substance concentration in the precursor solution ($C_{sol}$), Droplet diameter (d), nanocomposite particle diameter (D), frequency of the ultrasonic generator ($f$), Averaged molar mass of the nanocomposite particles ($M_{par}$), Molar mass of the precursor solution ($M_{pre}$), Surface tension of water ($\gamma$), density of the precursor solution ($\rho_{sol}$), Averaged density of the nanocomposite particles ($\rho_{par}$)

## References

1. Veleva, L.; Diaz-Ballote, L.; Wipf, D.O. An In Situ Electrochemical Study of Electrodeposited Nickel and Nickel-Yttrium Oxide Composite Using Scanning Electrochemical Microscopy. *J. Electrochem. Soc.* **2003**, *150*, C1, doi:10.1149/1.1522722.
2. Adekoya, J. A., Ogunniran, K. O., Siyanbola, T. O., Dare, E. O., Revaprasadu, N. Band Structure, Morphology, Functionality, and Size- Dependent Properties of Metal Nanoparticles. In *Noble and Precious Metals - Properties, Nanoscale Effects and Applications*; Seehra, M. S., Bristow, A.D., Ed.; IntechOpen, 2018; pp. 15–42.
3. Hamidi, R.; Ghasemi, S.; Hosseini, S.R. Ultrasonic Assisted Synthesis of Ni3(VO4)2-Reduced Graphene Oxide Nanocomposite for Potential Use in Electrochemical Energy Storage. *Ultrason. Sonochem.* **2020**, *62*, 104869, doi:10.1016/j.ultsonch.2019.104869.
4. Lou, B.S.; Rajaji, U.; Chen, S.M.; Chen, T.W. A Simple Sonochemical Assisted Synthesis of NiMoO4/Chitosan Nanocomposite for Electrochemical Sensing of Amlodipine in Pharmaceutical and Serum Samples. *Ultrason. Sonochem.* **2020**, *64*, 104827, doi:10.1016/j.ultsonch.2019.104827.
5. Abdullah, B.; Abd Ghani, N.A.; Vo, D.V.N. Recent Advances in Dry Reforming of Methane over Ni-Based Catalysts. *J. Clean. Prod.* **2017**, *162*, 170–185, doi:10.1016/j.jclepro.2017.05.176.
6. Aramouni, N.A.K.; Touma, J.G.; Tarboush, B.A.; Zeaiter, J.; Ahmad, M.N. Catalyst Design for Dry Reforming of Methane: Analysis Review. *Renew. Sustain. Energy Rev.* **2018**, *82*, 2570–2585, doi:10.1016/j.rser.2017.09.076.

7. Abdulrasheed, A.; Jalil, A.A.; Gambo, Y.; Ibrahim, M.; Hambali, H.U.; Shahul Hamid, M.Y. A Review on Catalyst Development for Dry Reforming of Methane to Syngas: Recent Advances. *Renew. Sustain. Energy Rev.* **2019**, *108*, 175–193, doi:10.1016/j.rser.2019.03.054.
8. 8Islam, M.H.; Burheim, O.S.; Pollet, B.G. Sonochemical and Sonoelectrochemical Production of Hydrogen. *Ultrason. Sonochem.* **2019**, *51*, 533–555, doi:https://doi.org/10.1016/j.ultsonch.2018.08.024.
9. Sun, G.B.; Hidajat, K.; Wu, X.S.; Kawi, S. A Crucial Role of Surface Oxygen Mobility on Nanocrystalline Y2O3 Support for Oxidative Steam Reforming of Ethanol to Hydrogen over Ni/Y2O3 Catalysts. *Appl. Catal. B Environ.* **2008**, *81*, 303–312, doi:10.1016/j.apcatb.2007.12.021.
10. Li, Y.; Men, Y.; Liu, S.; Wang, J.; Wang, K.; Tang, Y.; An, W.; Pan, X.; Li, L. Remarkably Efficient and Stable Ni/Y2O3 Catalysts for CO2 Methanation: Effect of Citric Acid Addition. *Appl. Catal. B Environ.* **2021**, *293*, 120206, doi:10.1016/j.apcatb.2021.120206.
11. Taherian, Z.; Khataee, A.; Orooji, Y. Facile Synthesis of Yttria-Promoted Nickel Catalysts Supported on MgO-MCM-41 for Syngas Production from Greenhouse Gases. *Renew. Sustain. Energy Rev.* **2020**, *134*, 110130, doi:10.1016/j.rser.2020.110130.
12. Guo, K.; Li, H.; Yu, Z. Size-Dependent Catalytic Activity of Monodispersed Nickel Nanoparticles for the Hydrolytic Dehydrogenation of Ammonia Borane. *ACS Appl. Mater. Interfaces* **2018**, *10*, 517–525, doi:10.1021/acsami.7b14166.
13. Rahemi Ardekani, S.; Sabour Rouh Aghdam, A.; Nazari, M.; Bayat, A.; Yazdani, E.; Saievar-Iranizad, E. A Comprehensive Review on Ultrasonic Spray Pyrolysis Technique: {Mechanism}, Main Parameters and Applications in Condensed Matter. *J. Anal. Appl. Pyrolysis* **2019**, *141*, 104631, doi:10.1016/j.jaap.2019.104631.
14. Li, C.; Hsieh, J.H.; Hung, M.; Huang, B.Q.; Song, Y.L.; Denayer, J.; Aubry, P.; Bister, G.; Spronck, G.; Colson, P.; et al. Ultrasonic Spray Pyrolysis for Nanoparticles Synthesis. *J. Mater. Sci.* **2004**, *9*, 3647–3657.
15. Švarc, T.; Stopić, S.; Jelen, Ž.; Zadravec, M.; Friedrich, B.; Rudolf, R. Synthesis of Ni/Y2O3 Nanocomposite through USP and Lyophilisation for Possible Use as Coating. *Materials (Basel).* **2022**, *15*, 1–17, doi:10.3390/ma15082856.
16. Majerič, P.; Rudolf, R. Advances in Ultrasonic Spray Pyrolysis Processing of Noble Metal Nanoparticles-Review. *Materials (Basel).* **2020**, *13*, doi:10.3390/MA13163485.
17. Pyrolysis, S.; Synthesis, O.; Mihailovi, M.; Stevanovi, J. Characterization of Defined Pt Particles Prepared by Ultrasonic. **2022**, *2*.
18. Shih, S.J.; Tzeng, W.L.; Jatnika, R.; Shih, C.J.; Borisenko, K.B. Control of Ag Nanoparticle Distribution Influencing Bioactive and Antibacterial Properties of Ag-Doped Mesoporous Bioactive Glass Particles Prepared by Spray Pyrolysis. *J. Biomed. Mater. Res. - Part B Appl. Biomater.* **2015**, *103*, 899–907, doi:10.1002/jbm.b.33273.
19. Golub, D.; Ivanič, A.; Majerič, P.; Tiyyagura, H.R.; Anžel, I.; Rudolf, R. Synthesis of Colloidal Au Nanoparticles through Ultrasonic Spray Pyrolysis and Their Use in the Preparation of Polyacrylate-AuNPs' Composites. *Materials (Basel).* **2019**, *12*, 1–17, doi:10.3390/ma12223775.
20. Shariq, M.; Marić, N.; Gorše, G.K.; Kargl, R.; Rudolf, R. Synthesis of Gold Nanoparticles with Ultrasonic Spray Pyrolysis and Its Feasibility for Ink-Jet Printing on Paper. *Micro Nanosyst.* **2018**, *10*, 102–109, doi:10.2174/1876402910666180802113859.
21. Majerič, P.; Jenko, D.; Friedrich, B.; Rudolf, R. Formation of Bimetallic Fe/Au Submicron Particles with Ultrasonic Spray Pyrolysis. *Metals (Basel).* **2018**, *8*, doi:10.3390/met8040278.
22. Shariq, M.; Majerič, P.; Friedrich, B.; Budic, B.; Jenko, D.; Dixit, A.R.; Rudolf, R. Application of Gold(III) Acetate as a New Precursor for the Synthesis of Gold Nanoparticles in PEG Through Ultrasonic Spray Pyrolysis. *J. Clust. Sci.* **2017**, *28*, 1647–1665, doi:10.1007/s10876-017-1178-0.
23. Jelen, Ž.; Majerič, P.; Zadravec, M.; Anžel, I.; Rakuša, M.; Rudolf, R. Study of Gold Nanoparticles' Preparation through Ultrasonic Spray Pyrolysis and Lyophilisation for Possible Use as Markers in LFIA Tests. *Nanotechnol. Rev.* **2021**, *10*, 1978–1992, doi:10.1515/ntrev-2021-0120.
24. Majerič, P.; Feizpour, D.; Friedrich, B.; Jelen, Ž.; Anžel, I.; Rudolf, R. Morphology of Composite Fe@Au Submicron Particles, Produced with Ultrasonic Spray Pyrolysis and Potential for Synthesis of Fe@Au Core-Shell Particles. *Materials (Basel).* **2019**, *12*, 10–12, doi:10.3390/ma12203326.
25. Rudolf, R.; Majerič, P.; Štager, V.; Albreht, B. The Process of Production Gold Nanoparticles with Modified Ultrasonic Spray Pyrolysis.
26. Gurmen, S.; Guven, A.; Ebin, B.; Stopić, S.; Friedrich, B. Synthesis of Nano-Crystalline Spherical Cobalt-Iron (Co-Fe) Alloy Particles by Ultrasonic Spray Pyrolysis and Hydrogen Reduction. *J. Alloys Compd.* **2009**, *481*, 600–604, doi:10.1016/j.jallcom.2009.03.046.
27. Özcelik, D.Y.; Ebin, B.; Stopic, S.; Gürmen, S.; Friedrich, B. Mixed Oxides NiO/ZnO/Al2O3 Synthesized in a Single Step via Ultrasonic Spray Pyrolysis (USP) Method. *Metals (Basel).* **2022**, *12*, doi:10.3390/met12010073.
28. Stopic, S.; Friedrich, B.; Schroeder, M.; Weirich, T.E. Synthesis of TiO2 Core/RuO2 Shell Particles Using Multistep Ultrasonic Spray Pyrolysis. *Mater. Res. Bull.* **2013**, *48*, 3633–3635, doi:10.1016/j.materresbull.2013.05.050.
29. Köroğlu, M.; Ebin, B.; Stopic, S.; Gürmen, S.; Friedrich, B. One Step Production of Silver-Copper (Agcu) Nanoparticles. *Metals (Basel).* **2021**, *11*, 1–11, doi:10.3390/met11091466.
30. Bang, J.H.; Suslick, K.S. Applications of Ultrasound to the Synthesis of Nanostructured Materials. *Adv. Mater.* **2010**, *22*, 1039–1059, doi:10.1002/adma.200904093.
31. Majerič, P.; Jenko, D.; Friedrich, B.; Rudolf, R. Formation Mechanisms for Gold Nanoparticles in a Redesigned Ultrasonic Spray Pyrolysis. *Adv. Powder Technol.* **2017**, *28*, 876–883, doi:10.1016/j.apt.2016.12.013.

32. Shih, S.J.; Wu, Y.Y.; Chen, C.Y.; Yu, C.Y. Morphology and Formation Mechanism of Ceria Nanoparticles by Spray Pyrolysis. *J. Nanoparticle Res.* **2012**, *14*, doi:10.1007/s11051-012-0879-4.
33. Winkler, N.; Wibowo, R.A.; Kautek, W.; Dimopoulos, T. Influence of the Aqueous Solution Composition on the Morphology of Zn1−xMgxO Films Deposited by Spray Pyrolysis. *J. Mater. Chem. C* **2019**, *7*, 3889–3900, doi:10.1039/c8tc06097e.
34. Wright, L.D.; Lowe, J.C.; Bliss, M.; Tsai, V.; Togay, M.; Betts, T.R.; Walls, J.M.; Malkov, A. V.; Bowers, J.W. Water Based Spray Pyrolysis of Metal-Oxide Solutions for Cu2ZnSn(S,Se)4 Solar Cells Using Low Toxicity Amine/Thiol Complexants. *Thin Solid Films* **2019**, *669*, 588–594, doi:10.1016/j.tsf.2018.11.040.
35. Varničić, M.; Pavlović, M.M.; Pantović, S.E.; Mihailović, M.; Pantović Pavlović, M.R.; Stopić, S.; Friedrich, B. Spray-Pyrolytic Tunable Structures of Mn Oxides-Based Composites for Electrocatalytic Activity Improvement in Oxygen Reduction. *Metals (Basel).* **2022**, *12*, doi:10.3390/met12010022.
36. Stopić, S.; Ilić, I.; Uskoković, D. Structural and Morphological Transformations during NiO and Ni Particles Generation from Chloride Precursor by Ultrasonic Spray Pyrolysis. *Mater. Lett.* **1995**, *24*, 369–376, doi:10.1016/0167-577X(95)00121-2.
37. Trenkenschuh, E.; Friess, W. Freeze-Drying of Nanoparticles: How to Overcome Colloidal Instability by Formulation and Process Optimization. *Eur. J. Pharm. Biopharm.* **2021**, *165*, 345–360, doi:10.1016/j.ejpb.2021.05.024.
38. Chen, G.; Wang, W. Role of Freeze Drying in Nanotechnology. *Dry. Technol.* **2007**, *25*, 29–35, doi:10.1080/07373930601161179.
39. Takenaka, S.; Shimizu, T.; Otsuka, K. Complete Removal of Carbon Monoxide in Hydrogen-Rich Gas Stream through Methanation over Supported Metal Catalysts. *Int. J. Hydrogen Energy* **2004**, *29*, 1065–1073, doi:https://doi.org/10.1016/j.ijhydene.2003.10.009.
40. Hasan, M.; Asakoshi, T.; Muroyama, H.; Matsui, T.; Eguchi, K. CO2methanation Mechanism over Ni/Y2O3: Anin Situdiffuse Reflectance Infrared Fourier Transform Spectroscopic Study. *Phys. Chem. Chem. Phys.* **2021**, *23*, 5551–5558, doi:10.1039/d0cp06257j.
41. Wang, B. Recent Development of Non-Platinum Catalysts for Oxygen Reduction Reaction. *J. Power Sources* **2005**, *152*, 1–15, doi:https://doi.org/10.1016/j.jpowsour.2005.05.098.
42. Lano, J. Ultrasonic Atomization of Liquids. *Acustica* **1962**, *341*, 28–30.
43. Dittrich, R.; Stopić, S.; Friedrich, B. *Mechanism of Nanogold Formation by Ultrasonic Spray Pyrolysis*; 2011; Vol. 3;.
44. Amis, T.M.; Renukuntla, J.; Bolla, P.K.; Clark, B.A. Selection of Cryoprotectant in Lyophilization of Progesterone-Loaded Stearic Acid Solid Lipid Nanoparticles. *Pharmaceutics* **2020**, *12*, 1–15, doi:10.3390/pharmaceutics12090892.
45. Dzimitrowicz, A.; Jamroz, P.; Greda, K.; Nowak, P.; Nyk, M.; Pohl, P. The Influence of Stabilizers on the Production of Gold Nanoparticles by Direct Current Atmospheric Pressure Glow Microdischarge Generated in Contact with Liquid Flowing Cathode. *J. Nanoparticle Res.* **2015**, *17*, doi:10.1007/s11051-015-2992-7.
46. Abdelwahed, W.; Degobert, G.; Stainmesse, S.; Fessi, H. Freeze-Drying of Nanoparticles: Formulation, Process and Storage Considerations. *Adv. Drug Deliv. Rev.* **2006**, *58*, 1688–1713, doi:10.1016/j.addr.2006.09.017.
47. ISO 527-2:2012 Plastics — Determination of Tensile Properties — Part 2: Test Conditions for Moulding and Extrusion Plastics 2012.
48. Schneider, C.A.; Rasband, W.S.; Eliceiri, K.W. NIH Image to ImageJ: 25 Years of Image Analysis. *Nat. Methods* **2012**, *9*, 671–675, doi:10.1038/nmeth.2089.
49. ISO 527-1:2019 Plastics — Determination of Tensile Properties — Part 1: General Principles 2019.
50. ASTM D5418-15 Standard Test Method for Plastics: Dynamic Mechanical Properties: In Flexure (Dual Cantilever Beam) 2015.
51. Arnipally, S.K.; Kuru, E. Settling Velocity of Particles in Viscoelastic Fluids: A Comparison of the Shear-Viscosity and Elasticity Effects. *SPE J.* **2018**, *23*, 1689–1705, doi:10.2118/187255-PA.
52. Krasnou, I.; Tarabukina, E.; Melenevskaya, E.; Filippov, A.; Aseyev, V.; Hietala, S.; Tenhu, H. Rheological Behavior of Poly(Vinylpyrrolidone)/Fullerene C60 Complexes in Aqueous Medium. *J. Macromol. Sci. Part B* **2008**, *47*, 500–510, doi:10.1080/00222340801955289.
53. Singh, M.; Kumar, S. Viscometric Studies of Poly(N-Vinyl-2-Pyrrolidone) in Water and in Water and 0.01% Bovine Serum Albumin at 283.15, 288.15, 293.15, 298.15, 303.15, 308.15, and 313.15 K. *J. Appl. Polym. Sci.* **2003**, *87*, 1001–1015, doi:https://doi.org/10.1002/app.11442.